Flame morphology and laminar flame assessments affected by flames interaction using multi-ignition sources of NH$_3$/H$_2$-air flames

Ahmed Yasiry [a,b], Jinhua Wang [a,*], Hongchao Dai [a], Xiao Cai [a], Ahmed A.A. Abdulraheem [c], Saba Y. Ahmed [c], Haroun A.K. Shahad [c], Zuohua Huang [a]

[a] State Key Laboratory of Multiphase Flow in Power Engineering, Xi'an Jiaotong University, Xi'an, 710049, China
[b] Automotive Engineering Department, College of Engineering-Musaib, University of Babylon, Babil, 51002, Iraq
[c] Mechanical Engineering Department, College of Engineering, University of Babylon, Babil, 51002, Iraq

A B S T R A C T

A detailed assessment of flame–flame interaction and laminar flame evolution using multi-ignition sources is experimentally studied. To understand the flame interaction, the centrally ignited flame is measured and calculated for comparison with multi-ignition sources hydrogen–ammonia/flame. The location of the external ignition source, the delay time, the hydrogen blending, and the mixture equivalence ratio at an initial pressure of 0.1 MPa affect the propagation and morphology of the flame. It can be observed that the advancement of the pressure wave of the external flame causes deformation to the central flame front; This deformation occurs even before the interaction of the flames. The deformation can be decomposed into horizontal deformation, which decelerates the flame front as a result of the drag or accelerates due to the thrust of the flow field on the flame front. At the same time, vertical deformation is influenced by drag and thrust-lift forces. Therefore, the equivalent flame decelerates with time. This effect gives a nonsymmetric shape for expanding flame, and the shape changes from spherical to ellipsoidal, then a triaxial quasi-ellipsoid flame (scalene). The equivalent flame speed and laminar burning velocity are maximized near stoichiometry for all delay times and locations of the ignition source. As the delay time of the stoichiometric hydrogen ammonia/air increases, the equivalent laminar flame speed and laminar burning velocity monotonously decrease, as well as the time and location of the interaction. The equivalent flame speed and laminar burning velocity for ignition sources 1 and 2 decreases with delay time, and this becomes evident on the rich side. While employing a third ignition source increases with delay time since the drag force get eliminated from the horizontal axis. Furthermore, the hydrogen blending effect enhances and highlights these tendencies.

1. Introduction

Combustion has been the dominant energy conversion strategy for human and industrial activities such as energy production and transportation since the industrial revolution. These applications tend to be crucially dependent on hydrocarbon fuels, where significant Carbon Dioxide (CO$_2$) emissions are adopted to be the primary contributors to global warming and climate change. Increasing concerns about renewable, low- or no-carbon fuels utilizing energy and power applications are essential to reduce CO$_2$ emissions for easing the progression effects of global warming, fossil fuel shortage, and an intensifying energy deficiency. Hydrogen (H$_2$) and ammonia (NH$_3$) have been suggested as renewable and clean energy sources (carbon-free fuels) and energy carriers to store and transport renewable energy sources [1].

Ammonia is easily transportable and stored fuel because of liquefaction characteristics compared with hydrogen; since H$_2$, and NH$_3$ require a temperature of –33.4 °C and –252.9 °C to be liquefied at atmospheric pressure [2]; otherwise, at room temperature, H$_2$ and NH$_3$ require 350–700 and 8.5 bar, respectively [3]. H$_2$ also has a wide range of flammability limits (0.1–7.1) and a faster Laminar Burning Velocity (LBV), approximately 2.91 m/s at ϕ = 1.7 and 0.07 m/s at ϕ = 1.05 for NH$_3$ at atmospheric conditions [1,4]. More considerable ammonia's hydrogen density (121 kg — H$_2$/m^3) compared to liquid hydrogen (70.8 kg — H$_2$/m^3) and hydrogen content (17.8% by weight of hydrogen); NH$_3$ is a more practical alternative fuel for different energy application [5]. Literature review articles [1,4,6–8] provide a summary of the advancements in ammonia applications, especially in the area of the most recent comprehension of ammonia combustion.

Increasing the combustion intensity is needed to make ammonia burn in gas turbines and engines. Several suggestions and research have

---

already been suggested to improve the combustion characteristics of ammonia, Such strategies as different fuels blend ammonia, i.e., co-firing, with a more reactive fuel, like hydrogen, methane, syngas, and oxygenated fuel, or oxidizer enhancement approach typically centers around replacing air with an oxygen-enriched mixture. Finally, increasing turbulence wrinkles the flames, which increases the flame surface density and, in turn, increases flame speed relative to the laminar burning velocity.

Recent developments in Internal Combustion Engines (ICEs) boosted energy density and fuel consumption and have been challenged by a new mode of engine knock, unwanted pre-ignition, developing detonation, or subsequent front propagation [9]. Knocking combustion is a common problem found in hydrogen-fueled engines [10]. Hydrogen has a small quenching distance and a minimum ignition energy roughly one order of magnitude lower than conventional fuels, therefore its flame may quickly autoignite and backfire into the intake manifold around a mostly closed intake valve. Hydrogen engines also knock. The cause of 'uncontrolled' autoignition is loading. A fuel with a high Research Octane Number (RON ≥ 130) may not knock, however hydrogen does not satisfy the typical criteria [11]. The knock tendency in a spark ignition engine is the most significant barrier to increasing its thermal efficiency that prevents engines from reaching optimal combustion phasing and a higher compression ratio. Due to this reason, a comprehensive understanding of knock-in high-efficiency engines is crucial to satisfy the upcoming regulations for fuel economy and pollution levels. Knock is the noise produced due to the auto-ignition of a portion of the fuel–air mixture before the propagating flame front. The abnormal combustion, temperature, cylinder pressure traces, and flame propagation velocity in the combustion chamber are the primary features of this condition [12]. Auto-ignition and detonation are two recognized hypotheses for knock. The auto-ignition hypothesis is based on the instantaneous igniting hot spots in the unburned end gas. This hypothesis explains the knock from a chemical kinetics viewpoint, with low temperature and rapid unburned end gas heat release. According to detonation theory, knocking is the combustion of an unburned mixture ahead of the regular flame front by strong pressure waves or shock waves. This hypothesis proposes that knock is caused by combustion flame with gas dynamics. There is no difference in the fundamentals between the two theories, only different research viewpoints. The first describes hot spot formation in the end-gas region, while the latter describes turbulent flame propagation and gas dynamics after auto-ignition. Several researchers have extensively studied the relationship of propagation characteristics between the pressure waves and auto-ignited flame, demonstrating that interaction is achievable when the velocities are the same [12–15]. Extensive efforts by researchers to examine and analyze the combustion process with multi-ignition sources [16,17] and obstacle positions that affect flame morphology [18,19]. Besides, researchers examined flame interactions utilizing various combustion configurations, and flame interactions that can be categorized as flame-shock or pressure wave interaction, flame–flame interaction, flame-turbulence interaction, flame–acoustic interaction, flame–wall interaction, and flame boundary layer interaction (tulip flame). [14,15,20–26].

Xiao et al. [19] studied the dynamics of a premixed hydrogen–air mixture ignited at different positions in a discrete closed tube. The flame performed differently depending on the ignition location. Tulip flame dynamics matched the theory when the ignitor was at the end. Flame oscillations were weak due to flame pressure wave interaction. The flame propagated more slowly and could not create a tulip flame when the ignition source was in the center. It also explained and modeled tulip flame formation using the pressure wave, viscosity or vorticity effect, and hydrodynamic instability. Bradly et al. [27] demonstrated how the chemical energy generated by an auto-ignition occurs through traveling pressure or shock waves generated by hot spots. When the waves reach the cylinder wall, they might have had an acoustic effect on the thermodynamic parameters of the neighboring end-gas. The mixture behind the wavefront may have been compressed enough to respond quickly, sending pressure pulses ahead to maintain these waves' propagation.

Hariharan and Wichmas [16] presented an experimental and numerical investigation of premixed flame propagation in a constant-volume combustion chamber $5 * 5$ cm cross-section and 30 cm depth using two spark plugs mounted on both ends with a delay time of 0, 10, 20, 25, 30, 40, 50, 60, 75, 85, and 110 ms. It was found that the flame front morphology changed from spherical expanding flame to fingering, then planer, and then tulip flame front before the two flames interacted. Increasing the delay time will change the morphology if the flame is faster. Ignition was followed by an accelerating spherical flame front, which decelerated to form a tulip flame front. The previous observations that affect flame morphology have been studied, and well-reviewed [28].

Still, there is no literature on how flame-pressure wave and/or flame–flame interaction affect the flame morphology on laminar flame propagation in a constant volume chamber. The present work aims to investigate flame front evolution and the laminar flame parameter evaluation method caused by flame interaction. Flame assessments have been obtained at different equivalence ratios, hydrogen blending, the location of an ignition source, and delay time. Experiments examine the behavior and characteristics of premixed ammonia–hydrogen/air flame ignited at multi-ignition sources from different locations. This study examines hydrogen–ammonia combustion, so the framework is structured as follows; Section 1 presents an introduction to this study. Section 2 presents this study's experimental setup and procedure, also the data analysis method used in this study. While Section 3 presents the flame morphology and laminar flame assessment influenced flame interaction by multi-ignition sources. Section 4 summarizes the conclusion of the study. The final Section 5 shows suggestions for future work regarding this technique.

2. Experimental setup and methodology

Experiments were conducted on a specially modified Constant-Volume Chamber (CVC), as shown in Fig. 1. The laminar flame speed is directly measured from Schlieren images. The inner diameter, length, and thickness of the combustion chamber are 305, 400, and 10 mm, respectively, with an approximate volume of 29 L. Two optical quartz windows with a diameter of 120 mm and a thickness of 20 mm are positioned opposite each other. They can be used to visualize and record how a flame propagates. A Schlieren technique uses two plano-convex lenses, and a high-speed camera (AOS-QPRI) with a total frame rate of 16,000 and 1000×1000 pixels, but the setting used in this experiment is 600×600 pixels and 2500 FPS, with a total time of recording = 1.02 s, and a light source to visualize flame. A particular ignition system has been designed and constructed for this study to control the duration of ignition, the delay time (the time between two ignition sources), and the power delivered are all controlled to create a successful spark.

The first ignition source (CF) is located in the center of the combustion chamber, ignited by two electrodes with a diameter of 1 mm and a spark gap of 1.5 mm, and the flame speed is denoted as (c). Then, the second ignition source (ExF) is located on the wall of the combustion chamber with three different locations, as shown in Fig. 1-B. The first external flame source, (ExF_1), is located at $(-45°)$ on the right lower side of the combustion chamber; besides, the flame radius and speed from this source denoted as z_1 and $\dot{z}_1$, respectively. The second external flame source, (ExF_2), is located at $(+45°)$ on the right upper side of the combustion chamber; besides, the flame radius and speed from this source denoted as z_2 and $\dot{z}_2$, respectively, and the third external flame source (ExF_3) is located at $(-90°)$ on the bottom of the combustion chamber; besides, the flame radius and speed from this source denoted as z_3 and $\dot{z}_3$, respectively. Hydrogen, ammonia, and air are injected into
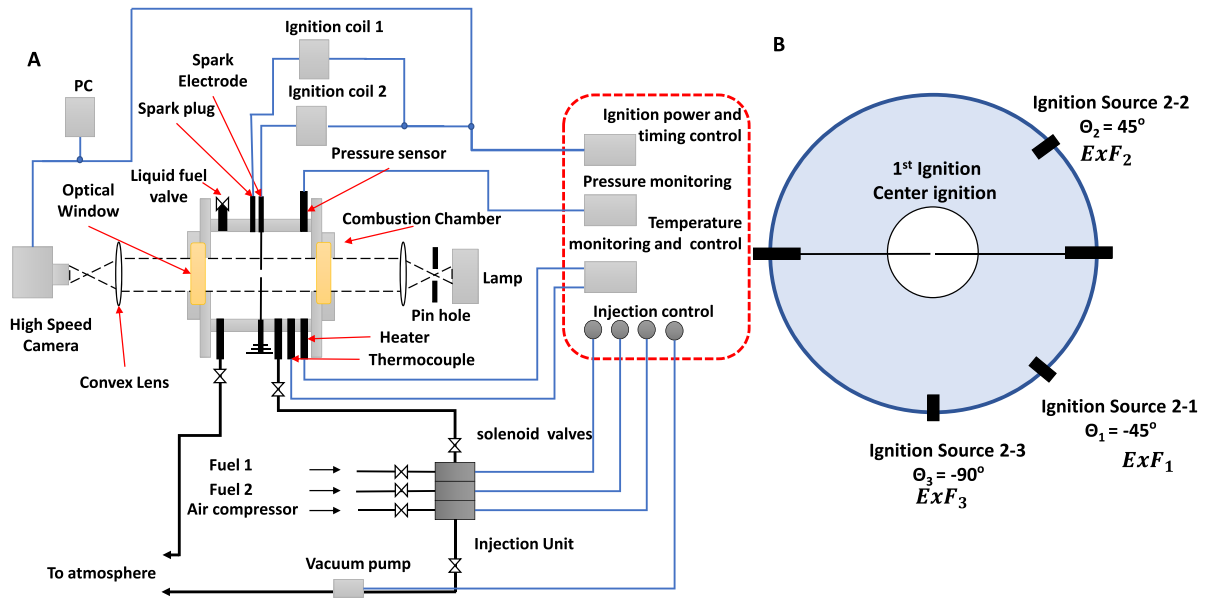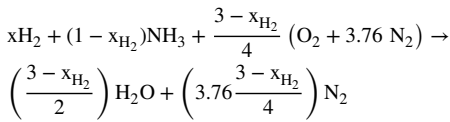
Fig. 1. A — Schematic of the experimental setup, B — front view for combustion chamber to illustrate the location of sparks plug fixed on the chamber's wall.

the combustion chamber synchronously using a four-way manifold with four solenoid valves. The fourth port is used for the vacuum.

All experiments were conducted at an initial temperature and pressure of 298 K and 0.1 MPa, respectively. The hydrogen addition to ammonia fuel was 20%–40% in volume, and the equivalence ratio is from 0.8 to 1.2, and five delay times 0–40 ms were used, as shown in Table 1. The combustion reaction follows the one-step global equation,

$$xH_2 + (1 - x_{H_2})NH_3 + \frac{3 - x_{H_2}}{4}\left(O_2 + 3.76\ N_2\right) \rightarrow$$
$$\left(\frac{3 - x_{H_2}}{2}\right)H_2O + \left(3.76\frac{3 - x_{H_2}}{4}\right)N_2$$

where x_{H_2} is the mole fraction for hydrogen and x_{NH_3} is the mole fraction for ammonia that equals $(1\text{-}x_{H_2})$, ϕ is the global equivalence ratio, which can be defined as:

$$\phi = \frac{\frac{x_{H_2} + x_{NH_3}}{x_{air}}}{\left(\frac{x_{H_2} + x_{NH_3}}{x_{air}}\right)_{st}}, \tag{1}$$

Matching the flames' interaction location within the glass window's visible area (measurement region) is crucial by synchronizing the following parameters; (1) the delay time, (2) the distance between the ignition sources (chamber radius), (3) the fuel's flame speed, and (4) the initial conditions (temperature, pressure, and equivalence ratio) as shown in Fig. 2-c. In this study, hydrogen blending was tested from 0%–60%. Still, the active blending ratios of 20%–40% have been chosen to guarantee that the interaction location occurred within the measurement region so that the flame had sufficient time to interact. Delay time should be increased when reducing the hydrogen blends and decreased when increasing the hydrogen blends by 40%. Each experiment starts with a vacuum to scavenge the residual gases and a flush to introduce the mixture. Then, the minor portion of the blending fuel is admitted from its storage tank to the chamber based on Gibbs–Dalton's law, and then air is admitted into the chamber. The initial pressure and temperature are measured, and after that, all valves are closed, the camera is set and the ignition timing of sources 1 and 2. Then, the delay time and ignition power are set. One trigger ignites the air–fuel mixture, records data, and takes photos of the propagating flame. The whole procedure of the experiment is mentioned in detail [29].

Significant attempts have been made to enhance the accuracy of reaction mechanisms, which rely on precise laminar flame speed measurements [30]. Current measurements' uncertain quantification depends on the procedures described in Ref. [31] using the combination

Table 1
Experimental conditions in this work.

Fuel type	Ignition sources	Delay time (ms)	Equivalence ratio
20H$_2$–80NH$_3$	C	0	[0.8–1.2] ($\Delta = 0.2$)
20H$_2$–80NH$_3$	C + ExF$_1$	[0–40] ($\Delta = 10$)	[0.8–1.2] ($\Delta = 0.2$)
20H$_2$–80NH$_3$	C + ExF$_2$	[0–40] ($\Delta = 10$)	[0.8–1.2] ($\Delta = 0.2$)
20H$_2$–80NH$_3$	C + ExF$_3$	[0–30] $\Delta = 10$	$\phi = 1$
40H$_2$–60NH$_3$	C; ExF$_1$	0	[0.8–1.2] ($\Delta = 0.2$)
40H$_2$–60NH$_3$	ExF$_2$; ExF$_3$	0	$\phi = 1$
40H$_2$–60NH$_3$	C + ExF$_1$	[0–40] ($\Delta = 10$)	[0.8–1.2] ($\Delta = 0.2$)
40H$_2$–60NH$_3$	C + ExF$_2$	[0–40] ($\Delta = 10$)	[0.8–1.2] ($\Delta = 0.2$)
40H$_2$–60NH$_3$	C + ExF$_3$	[0–30] $\Delta = 10$	$\phi = 1$

of the experimental facility's specifications and the precision of the selected processing techniques. The uncertainty is evaluated for the unstretched flame speed (S_S), not for LBV itself. The total uncertainty estimate is calculated using,

$$\Delta S_L = \sqrt{\left(B_R\right)^2 + \left(\frac{tS_R}{\sqrt{N}}\right)^2} \tag{2}$$

where B_R is the total bias uncertainty that can be analyzed according to the method used by Lhuillier et al. [32] for estimate the bias for initial temperature, pressure, equation ratios, extrapolation, bouncy, and radiation. The pressure transducer and thermocouple accuracy with an of were less than ± 0.1 KPa, and ± 2 K, respectively. Additionally, S_R is the standard deviation of N repeated measurement, and t is the Student's multiplier for 95% confidence; where $S_R = \sqrt{\frac{\sum_{i=1}^{N}(X_i - \bar{X})^2}{N-1}}$. The overall experimental uncertainties of S_L were evaluated as ± 0.6–5.1 cm/s.

2.1. Data processing and parameter evaluation methods

Using the flame area method to measure the laminar burning velocity, estimating the radius of a typical spherical, centrally ignited, outwardly propagating flame directly from the Schlieren photographs. Recorded data may be affected by two significant determinants. When the flame radius is less than 6 mm, the flame speed is influenced by ignition energy, but it is independent of ignition energy when the flame radius exceeds 6 mm [33]. In addition, the second determinant to the flame radius from which meaningful data may be taken. The chamber wall's influence may be ignored while the radius exceeds

40 mm (less than 0.3 times the radius of the wall [34]). In this study, the affected laminar flame speed is calculated using a flame radius of 6–40 mm for the direct method of spherically centrally ignited outwardly propagating flame stretched flame speed ($S_{n,c}$), which can be evaluated as follows;

$$S_{n,c} = \frac{dr_{sch}}{dt} \qquad (3)$$

where t is the progress time, and c denotes to the center location of the ignition source, r_{sch} is the flame radius estimated from the Schlieren images where $\left(r = \sqrt{\frac{A_F}{4\pi}} \right)$, where A_F is the flame area. Since the effects of flame stretch influence the spherically propagating flame, the flame stretch rate, α, was evaluated using the following equation;

$$\alpha = \frac{1}{A_F} \frac{dA_F}{dt} = \frac{2}{r_{sch}} \frac{dr_{sch}}{dt} = 2 \frac{S_{n,c}}{r} \qquad (4)$$

Regarding asymptotic analysis, the difference between S_s and $S_{n,c}$ can be considered to be proportional to the stretch rate, as shown by Eq. (5)

$$S_s - S_{n,c} = L_b \cdot \alpha \qquad (5)$$

where L_b is the burned gas Markstein length. Thus S_s can be calculated by the linear extrapolation of $\alpha \to 0$ (or $r_{sch} \to \infty$). Using the density of the burnt gas mixture ρ_b and ρ_u for the unburnt mixture, LBV is calculated by $S_l = \frac{\rho_b}{\rho_u} \cdot S_s$; where these densities are calculated using the thermal equilibrium by Chemkin-PRO.

The abovementioned procedure suits a centrally ignited single flame with spherical shapes and diameters from all almost identical axes. Even the buoyancy effect is present in some cases of spherically propagating flames with a normal LBV. Still, these upward and deformation velocities of the flame front induced by the buoyancy have a minor and insignificant effect and cannot deform the flame front. When the flame speed is deficient, or the two flames propagated in a closed system, the flame speed at different axes varies, especially in the vertical axis, when the buoyancy effect is present. As a result, the flame propagates with an oblate spheroid flame rather than a spherical flame. A cartesian coordinate system is used in which the spark gap is the center of the spheroid flame. The coordinate axes are the axes of the ellipsoid, where X, Y, and Z are positive real numbers where X (horizontal diameter), Y (vertical diameter), and Z (parallel to the second ignition source), as illustrated in Fig. 2 with the points (X, 0, 0), (0,Y,0), and (0,0,Z). If X = Y > Z, it is an oblate spheroid. If X = Y < Z, it is a prolate spheroid. It is a sphere when X = Y = Z [35]. The central flame (centrally propagating flame) can be affected by the bouncy effect and pressure wave initiated by the external flame (flame with the chamber's wall-mounted ignition source). These two effects deform the flame front from a spherical flame to a spheroid; then, it can be represented as a triaxial quasi-ellipsoid (with unequal diameters from three axes) flame to simplify flame analysis for flame interaction using multi-ignition sources as shown in Fig. 2. It can be noticed from Fig. 2 that the speed of propagation is not equal along the three axes, where the flame speed along the XX-axis is affected by the horizontal component of the external flame, where $S_{n,o}$ is the flame speed caused by an external flame. At the same time, the flame speed along the YY-axis is affected by the vertical component of the external flame and bouncy effect. Therefore, S_b is the vertical buoyancy-induced deformation flame speed, where S_{b1} and S_{b2} are the vertical buoyancy-induced deformation velocities at the upper and lower ends, respectively.

In this study, according to the location of the external flame, the flame front may accelerate from two sides and decrease from two opposite sides, as shown in Fig. 2. Owing to the symmetry of the combustion chamber, the locations of external flame are located on the right side of the chamber; hence, It can be noticed that the flame accelerated on the horizontal-left side (−X). Furthermore, the flame decelerated on the horizontal-right side (+X). It can be noticed in Fig. 2-b that the flame got accelerated from the left (−X) and up (+Y) and got

decelerated from the right side (+X) and downside (−Y). The equivalent diameter for the spherical flame is drawn by estimating the vertical and horizontal diameters of the flame passing the center of the flame. The variation rate in the horizontal and vertical diameters can be extracted from the Schlieren images, which are denoted by $\dot{x}$ and $\dot{y}$, respectively. The parameters $\dot{x}$ and $\dot{y}$ may be stated in a general form for three different locations of the first ignition source as follows;

$$\dot{x} = 2S_{n,c} - \left(\dot{z}_1\right)_x - \left(\dot{z}_2\right)_x \qquad (6)$$

$$\dot{y} = 2S_{n,c} + S_{b1} - S_{b2} - \dot{z}_3 - \left(\dot{z}_1\right)_y - \left(\dot{z}_2\right)_y \qquad (7)$$

The centrally equivalent spherical flame and the pressure wave-affected tri-axial quasi-ellipsoid flame have the same fuel consumption rate when compared to one another. Therefore, the volume and its increasing rate are both identical and can be written as;

$$\frac{4}{3}\pi r^3 = \frac{4}{3}\pi \left(\frac{X}{2} \frac{Y}{2} \frac{Z}{2} \right)$$

then,

$$r_{eq} = \frac{1}{2} X^{\frac{1}{3}} Y^{\frac{1}{3}} Z^{\frac{1}{3}} \qquad (8)$$

where r_{eq} is the equivalent radius of the equivalent spherical flame. From Eq. (3), the equivalent stretched laminar flame speed can be written as;

$$\begin{aligned} S_{n_{eq}} &= \frac{dr_{eq}}{dt} = \frac{d}{dt}\left(\frac{1}{2} X^{\frac{1}{3}} Y^{\frac{1}{3}} Z^{\frac{1}{3}} \right) \\ &= \frac{1}{2}\left(X^{\frac{1}{3}} \frac{d}{dt}\left(Y^{\frac{1}{3}} Z^{\frac{1}{3}} \right) \frac{1}{3} + \frac{1}{3} X^{\frac{-2}{3}} Y^{\frac{1}{3}} Z^{\frac{1}{3}} \dot{x} \right) \end{aligned}$$

Then, the equivalent stretched laminar flame speed can be written as;

$$S_{n_{eq}} = \frac{1}{6}\left[X^{\frac{-2}{3}} Y^{\frac{1}{3}} Z^{\frac{1}{3}} \dot{x} + X^{\frac{1}{3}} Y^{\frac{-2}{3}} Z^{\frac{1}{3}} \dot{y} + X^{\frac{1}{3}} Y^{\frac{1}{3}} Z^{\frac{-2}{3}} \dot{z} \right] \qquad (9)$$

The stretch rate of the corresponding equivalent spherical flame may be calculated using Eq. (4) as follows;

$$\alpha = \frac{\frac{1}{6}\left[X^{\frac{-2}{3}} Y^{\frac{1}{3}} Z^{\frac{1}{3}} \dot{x} + X^{\frac{1}{3}} Y^{\frac{-2}{3}} Z^{\frac{1}{3}} \dot{y} + X^{\frac{1}{3}} Y^{\frac{1}{3}} Z^{\frac{-2}{3}} \dot{z} \right]}{\frac{1}{2} X^{\frac{1}{3}} Y^{\frac{1}{3}} Z^{\frac{1}{3}}}$$

Then, the equivalent stretched rate can be written as;

$$\alpha = \frac{2}{3}\left[\frac{\dot{x}}{X} + \frac{\dot{y}}{Y} + \frac{\dot{z}}{Z} \right] \qquad (10)$$

For checking, if the propagating flame is typical spheroidal, then diameters from all sides are the same, the 2r = d = X = Y = Z, then in Eq. (8) to get radius $r = \frac{1}{2} d^{\frac{1}{3}} d^{\frac{1}{3}} d^{\frac{1}{3}}$ then, r = d/2. While the stretched flame speed from Eq. (9) can be rewritten to be identical to Eq. (3) for the stretch rate to get Eq. (4).

3. Results and discussions

3.1. Flame morphology

Normal centrally-ignited premixed laminar flames propagate spherically in all directions unless it may be exposed to hydrodynamic and diffusional-thermal instabilities [36] or a buoyancy effect [37] that distorts the flame's structure. An external source, such as an obstacle, may deform the flame morphology and propagation. These effects are entirely neglected, and the only effect is caused by the propagation of the external flame on the central flame front evolution of the main flame.

Fig. 3-A displays the influence of the position of the external flame propagation with a delay time of 10 ms advancing the initiation of the central flame at three locations for an equivalence ratio of 1.2 and hydrogen blend of 40%. The first snap is taken after 6 ms of the central spark's ignition, while the last photo for each case represents the interaction between the two flames. The second and third photos
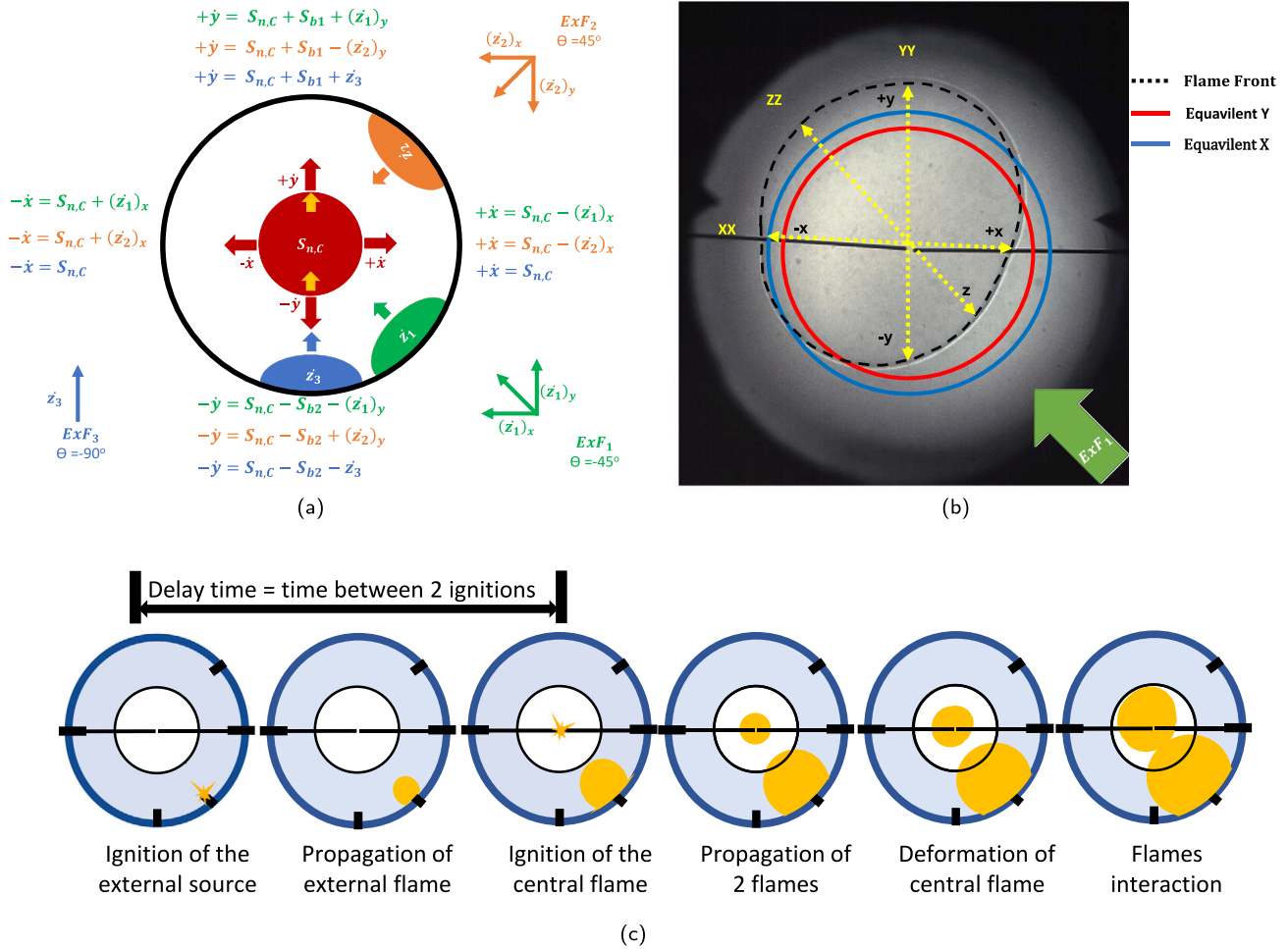
$$+\dot{y} = S_{n,C} + S_{b1} + (\dot{z_1})_y$$
$$+\dot{y} = S_{n,C} + S_{b1} - (\dot{z_2})_y$$
$$+\dot{y} = S_{n,C} + S_{b1} + \dot{z_3}$$

$$-\dot{x} = S_{n,C} + (\dot{z_1})_x$$
$$-\dot{x} = S_{n,C} + (\dot{z_2})_x$$
$$-\dot{x} = S_{n,C}$$

$$+\dot{x} = S_{n,C} - (\dot{z_1})_x$$
$$+\dot{x} = S_{n,C} - (\dot{z_2})_x$$
$$+\dot{x} = S_{n,C}$$

$$-\dot{y} = S_{n,C} - S_{b2} - (\dot{z_1})_y$$
$$-\dot{y} = S_{n,C} - S_{b2} + (\dot{z_2})_y$$
$$-\dot{y} = S_{n,C} - S_{b2} - \dot{z_3}$$

(a)

(b)

(c)

Fig. 2. Propagation and deformation of the Tri-axial quasi-ellipsoid expanding flame induced by bouncy and external flame effects at three locations. (a) Analysis of the flame speed in the four directions. (b) Triaxial quasi-ellipsoid flame and equivalent spherical expanding flame induced by ExF$_1$ flame effect. (c) Propagation, deformation, and interaction of the two expanding flames utilizing the first external ignition source.

are selected between the first and last at regular intervals. As the external flame is ignited, the pressure wave influences the propagation of the central flame. It dislodges the central flame in the opposite direction, creating a triaxial quasi-ellipsoid shape. This observation indicates that the morphology of the flame front is changing from spherical to elliptical and then from a triaxial quasi-ellipsoid shape. Before the flames interact, continuous cracks develop and begin to spread across the surface of the flame. These cracks refer to the formation of discontinuities or gaps in the flame front as it propagates through the combustible mixture. These cracks can develop due to various factors such as turbulence, heat loss, chemical reactions, and local variations in the fuel–air mixture. One way to understand the crack formation is through the concept of flame stretch. When an external flame propagates, the pressure wave varies the flow velocities and accelerations, leading to stretching and compression of the flame front. This stretching can cause the flame to become thinner in certain regions, leading to the formation of cracks as the flame propagates through the mixture. Fig. 3-B shows the flame behavior in three equivalence ratios using the first external flame source (ExF$_1$) with a 10 ms delay time and the hydrogen blend of 40%. The density ratio increases as the adiabatic flame temperature increases, as does the intensity of the hydrodynamic instability. Increasing the equivalence ratio increases the Lewis number (Le); hence, the thermal diffusion is greater than the mass diffusion. This effect has three influences; (1) increasing the flame speed due to increasing the thermal diffusion leading to a faster reaction rate. (2) Increasing Le leads to thinner flame fronts. This is because the increased thermal diffusion effect leads to faster mixing of fuel and

oxidizer, leading to a thinner flame front, increasing stability. (3) reducing the sensitivity to stretch since the flame became less likely to be extinguished by turbulence or other factors that cause the flame to be stretched. With an expansion and increasing density ratio, both flames grow more wrinkled. LBV maximized near stoichiometry, causing the external flame to propagate faster and be visualized earlier. It can be noticed from Fig. 5 that increasing hydrogen blends increases adiabatic flame temperature, Lewis number, hence, laminar burning velocity, and decreases thermal expansion ratio, which leads to a decrease in the hydrodynamic instability. For both hydrogen blends, the flame is unstable on the lean side and hydrodynamically stable toward the rich side. When the flame temperature increases due to the preferential diffusion of the reactant to heat conduction. Therefore, the local increase in flame speed due to increased flame temperature increases flame perturbation, consequently leading to thermal-diffusion instability. The flame evolution at five delay times utilizing the first external flame source (ExF$_1$) with a 40% hydrogen blend and an equivalence ratio of 1.2 are illustrated in Fig. 4-A. The first snap is taken after 6 ms of the central spark's ignition, while the last photo for each case represents the interaction between the two flames. The second and third photos are selected between the first and last at regular intervals. At an interaction instant, the higher the delay time, the farther the external flame spreads and the closer the interaction location to the center of the chamber. At a delay of 40 ms, the fastest the flame spreads, the earliest the central flame deforms, and the nearest to the center the flames interact. It can also notice that the flame front change from a spherical to a quasi-ellipsoidal shape. The evolution of the individual external flame
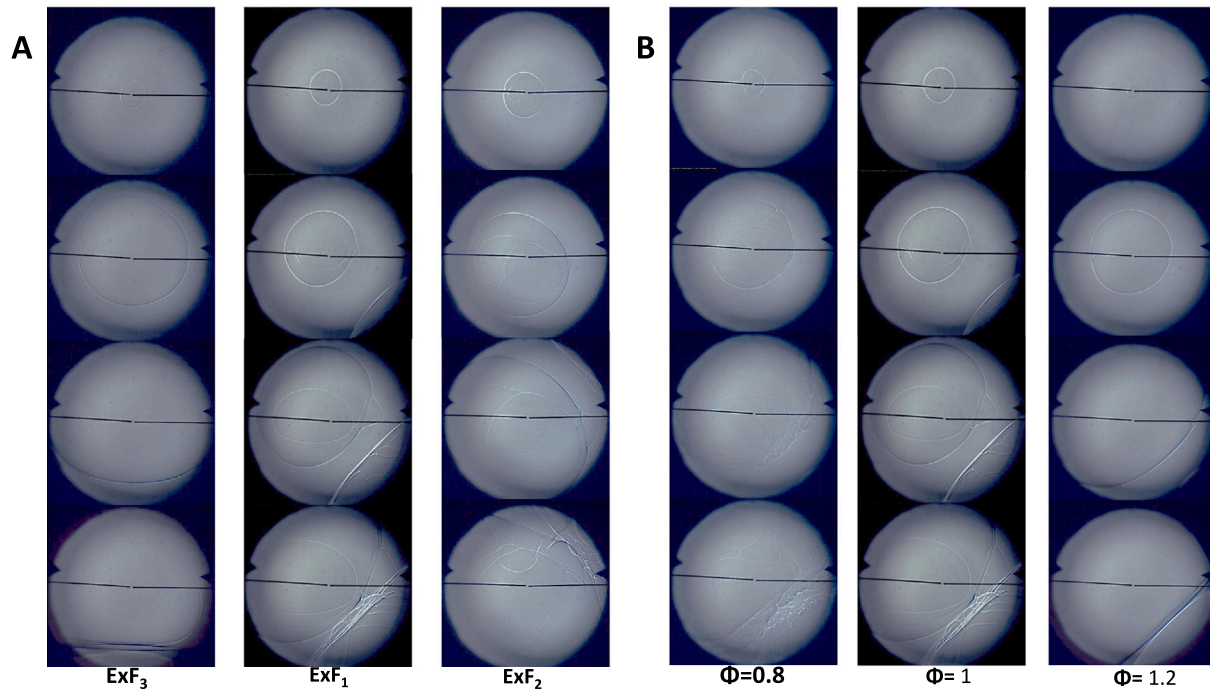
Fig. 3. Snapshots of the flame propagation for; A – 10 ms delay time at three various locations for an equivalence ratio = 1.2, the hydrogen concentration of 40%, the initial pressure of 1 atm and initial temperature of 298 K., and B – 10 ms delay time for ExF$_1$ at three various equivalence ratio, the hydrogen concentration of 40%, the initial pressure of 1 atm and initial temperature of 298 K.
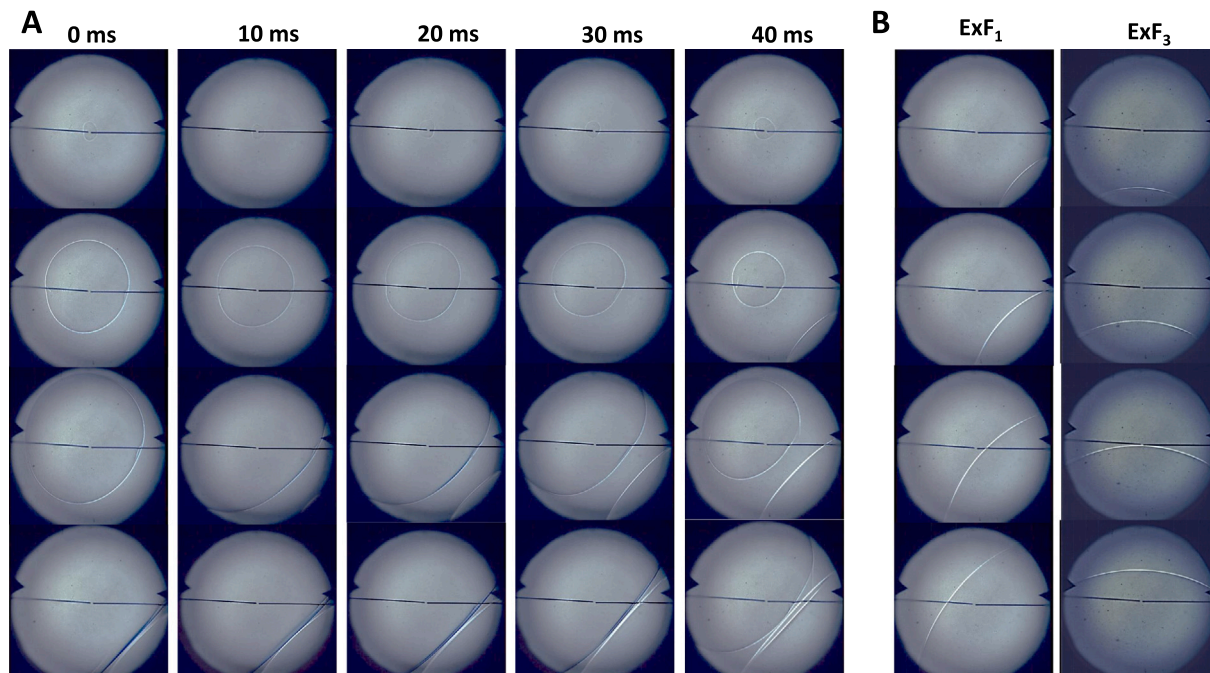

Fig. 4. Snapshots of the flame propagation for; A — An equivalence ratio of 1.2 at five different delay times for ExF$_1$, hydrogen concentration of 40%, the initial pressure of 1 atm and initial temperature of 298 K., and B — various single non-center flame at an equivalence ratio of 1.2, the hydrogen concentration of 40%, the initial pressure of 1 atm and initial temperature of 298 K.
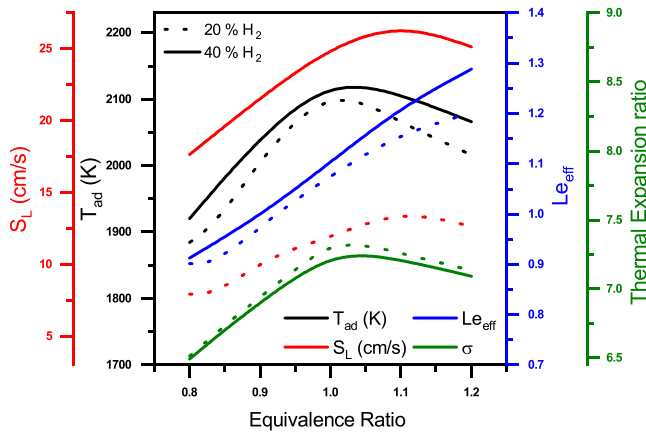
Fig. 5. Flame characteristics parameters with equivalence ratios at different hydrogen blending of 20% and 40%, the initial pressure of 1 atm and initial temperature of 298 K.
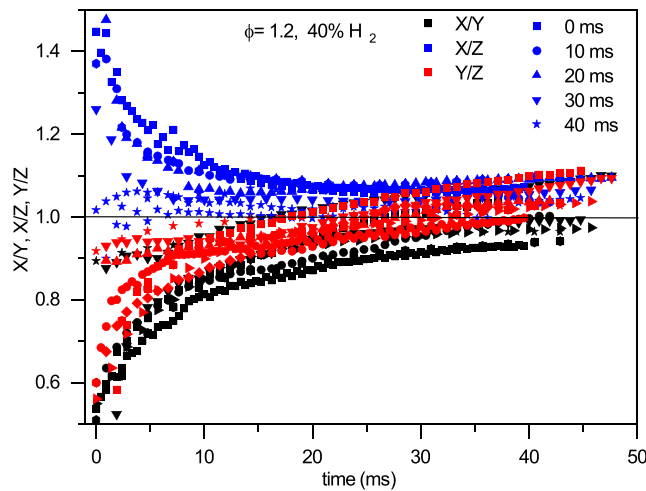

Fig. 6. Variation of the ratio of horizontal axis length to vertical axis length and diagonal axis length with time for ExF_1 flame and an equivalence ratio of 1.2, the hydrogen concentration of 40%, the initial pressure of 1 atm, and initial temperature of 298 K.

of (ExF_1 and ExF_3) without a central flame is shown in Fig. 4-B. It can be noticed that the (ExF_1) has a lower flame speed compared with (ExF_3 and S_{fc}) because of the bouncy effect and less effect of the cold chamber wall.

3.2. Flame front evolution

Images are analyzed to determine the diameters (X, Y, and Z), flame radius (x, y, and z), and the rate of change of the radius ($\dot{x}$, $\dot{y}$, and $\dot{z}$) along both sides of the three axes (XX, YY, and ZZ) of the tri-axial quasi-ellipsoid flame respectively.

Fig. 6 shows how the ratios of the ellipsoidal flame's three axial lengths (X/Z, X/Y, and Y/Z) vary over time. It can be seen that the ratio of the ellipsoidal flame's horizontal axial length to its vertical (X/Y) increases rapidly initially, where the flame becomes more oblate and then slowly when the flame becomes more prolate. First, the progress of (X/Z) goes down quickly (the flame becomes more prolate), and then it goes down slowly (the flame becomes more oblate). The ratio of X/Y is lesser than unity regardless of the time and more significant than unity for X/Z. In contrast, the ratio of Y/Z starts less than unity and increases gradually to pass the unity before the end of the propagation. The overall shape of the flame is a tri-axial quasi-ellipsoid. The uncertainty

in the measurement of the flame position is less than 3 Fig. 6 also shows the effect of delay time on the ratios of the ellipsoidal flame's three axial diameters (X/Z, X/Y, and Y/Z). Increasing the delay time above 20 ms stabilizes the ratios of axial length near unity because the effect of the pressure wave is already passed the initiation of the main flame. The impact of a non-symmetrical expanding flame on a three-axis system is shown from two perspectives. The first strategy involves decreasing the flame speed on the closest quarter of the ellipsoidal shape due to drag force, which is the dominant effect. In the second strategy, the flame speed increases due to the pressure wave causing lift and thrust forces in both directions. The asymmetrical length of the axes divides the projected view into two parts, the positive and negative. The horizontal axis (XX) is divided into the right and left sides radius. The flame speeds are denoted as ($+\dot{x}$, and $-\dot{x}$), respectively, while the vertical axis (YY) is divided into the up and downsides, and the flame speed for each side are ($+\dot{y}$, and $-\dot{y}$) respectively. The third axis (ZZ) also has two propagated flames that must be investigated. The first flame is one of the external flames, denoted as (z_1, z_2, and z_3), which refers to (ExF_1, ExF_2, and ExF_3, respectively), while the other flame propagating on this axis is the central flame parallel to the external flame and that will be denoted as $\dot{z}$ respectively.

The flame radius and the flame speed in different directions are illustrated in Fig. 7 for the central flame and the external flame (ExF_1) at different equivalence ratios (i – ϕ = 1.2, ii– ϕ = 1) and delay times of (0, and 30 ms). Fig. 7-A, C, E, and G present the radius of four directions versus time for expanding flame. Besides, the flame is assumed to be developed uniformly, equally, and non-deformity when the central expanding flame expands alone without external flame. In the beginning, the propagation of the center flame was smooth and uniform along all axes; however, when the external flame further propagated, the pressure wave influenced the neighboring layers, and the flame speed for both flames on the ZZ axis decreased, then got interacted. While the opposite side of the flame expands faster and gradually, non-uniformity can be seen. In a conventional centrally propagating flame, the flame outwardly expands due to diffusional and expansion effects; nonetheless, for multi-flames propagating in a closed chamber, the effect of the pressure wave decreases the flame speed at the closest part of the same axis as the external flame source, though increasing the flame speed in the opposite side as shown in Fig. 2. Increasing delay time induces the rate and starting time of the deformation, as shown in Fig. 7-A, and C, where 30 ms presents an earlier deformation compared with 0 ms. Fig. 7-G demonstrates an unusual structure of external flame propagation at the unity equivalence ratio. As the delay time exceeds 25 ms, the external flame appears to come through the glass window first before the central flame ignites.

3.3. Laminar flame speed and parameters of flame interactions

Fig. 7-B, D, F, and H illustrate the experimental stretched flame speed as a function of time using the first external flame (ExF_1) at delay times of 0 and 30 ms at different equivalence ratios. Besides, the centrally ignited flame speed is estimated using Eq. (3) at the same initial conditions, which is used to compare the propagation of multi flames. It is possible to observe a more remarkable decrease in the flame speed for the external flame as the delay time increases due to the pressure wave generated by the external flame. In addition, the flame speed of the external flame will decrease as progress time increases until the flames interact. When the delay time is zero, the flame speed of the external flame becomes steady because the flame speed of the ZZ-axis ($\dot{z}$) becomes constant and near zero flame speed. As the progress time increases, the speed of the equivalent flame becomes slower due to the effect of the external flame, which decreases the flame speed from the side opposing the direction of the propagation. For instance, under any initial conditions and while utilizing the first external flame source (ExF_1), the flame speeds ($+\dot{y}$, $-\dot{x}$) increase due to flame expanding, and they have the same direction of propagation with
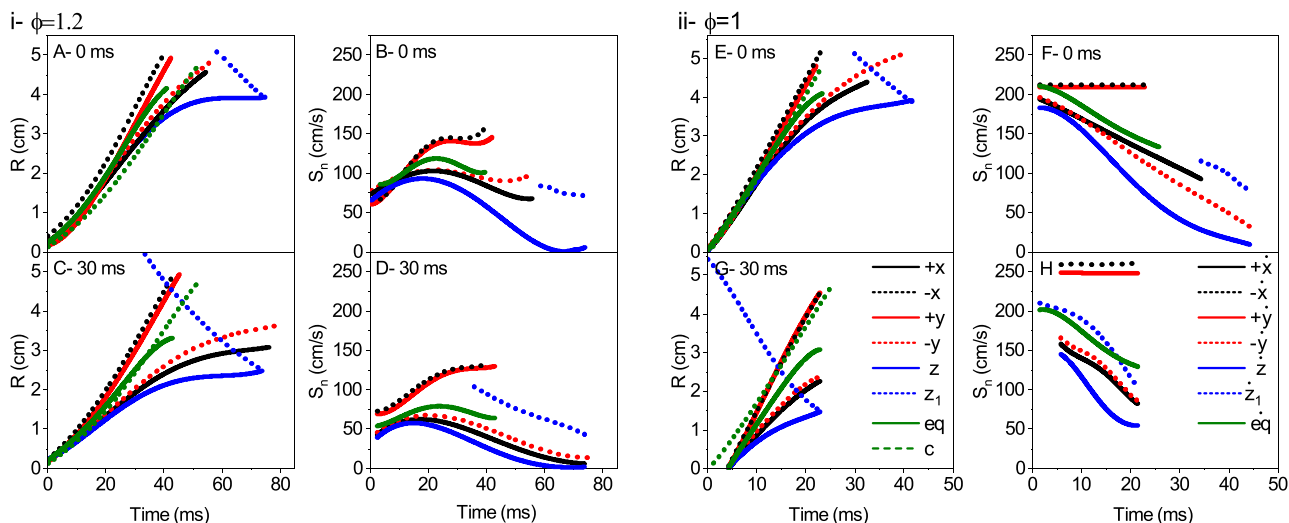
Fig. 7. Variation of the radius of the flame propagation with time utilizing ExF_1 flame at an equivalence ratio of 1.2 for the different delay times of A — 0 ms, C — 30 ms, and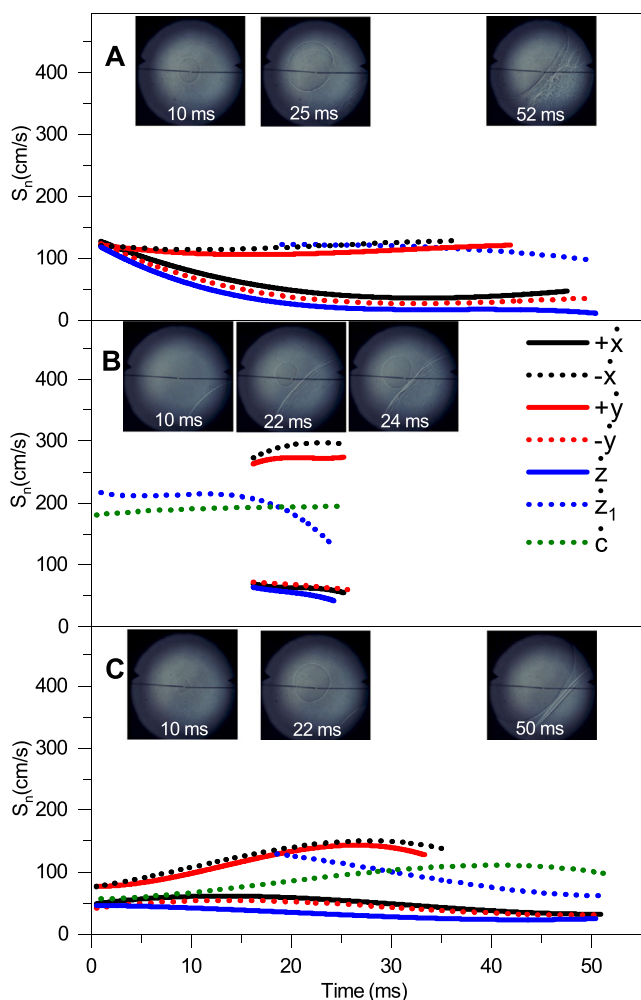 at an equivalence ratio of 1 for E — 0 ms, and G — 30 ms. While the variation of the laminar flame speed with time utilizing ExF_1 flame at an equivalence ratio of 1.2 for the different delay times of B — 0 ms, D — 30 ms, and at an equivalence ratio of 1 for F — 0 ms, and H — 30 ms.

Fig. 8. Propagation of flame versus time for −45° degree ExF_1 flame and for equivalence ratio of A — 0.8, B — 1, and C — 1.2, and hydrogen concentration of 40%, the initial pressure of 1 atm and initial temperature of 298 K.
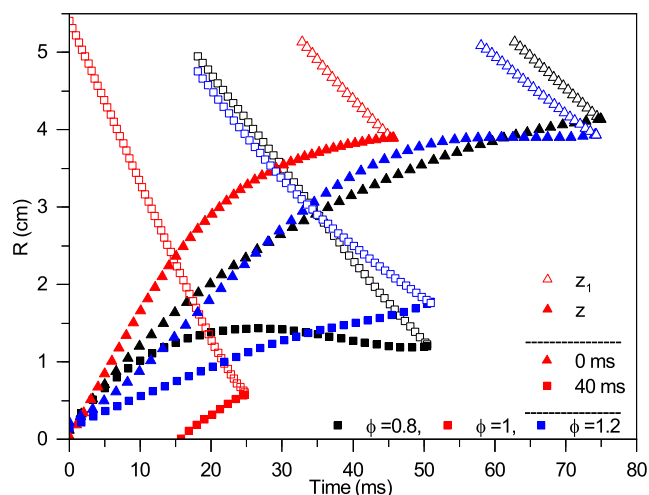

Fig. 9. Variation of the external radius to the parallel radius with time at different equivalence ratio for ExF_1 flame, and hydrogen concentration of 40%, the initial pressure of 1 atm and initial temperature of 298 K.

the external flame, while $(-\dot{y}, +\dot{x})$ decreases to low values due to flame reduction by a pressure wave that moves in the opposite direction of these flame; moreover, its values slopped negatively, and its value was lower than the value of a normal flame. Fig. 2 clarifies this phenomenon mathematically.

It can be noticed that the flame speed utilizing the third external flame source (ExF_3) will have faster flame speed since the effect of the ignition source is the fastest flame speed compared with others, also faster than a single central flame since the pressure wave effect in the same direction of the buoyancy effect.

Fig. 8 illustrates the effect of the equivalence ratio on the flame propagation over a delay time of 40 ms while utilizing the first external flame source (ExF_1) with three photos, where the first photo for 10 ms after the detection of the first flame and the second photo is 5 ms after the second flame appears, and then the last photo shows the two flames interacted, the fastest flame speed on the stoichiometry as shown in Fig. 8-B, where the external flame was observed initially, and after 17 ms, the central flame ignited as mentioned previously; as a result, the flame speed of $(+\dot{y}, -\dot{x})$ increased while $(-\dot{y}, +\dot{x})$ in a relatively
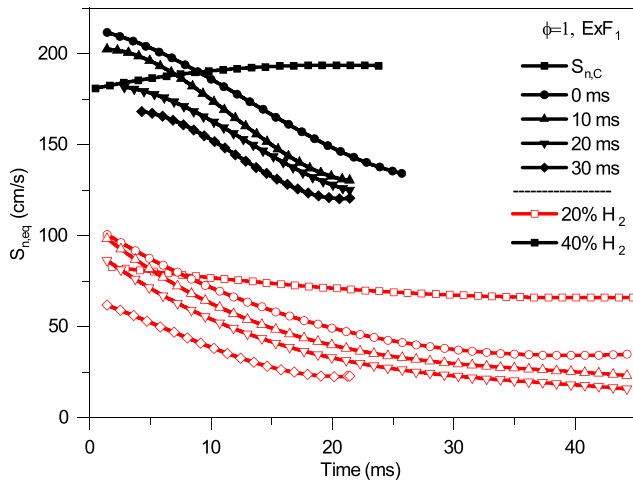
Fig. 10. The effect of delay time on the equivalent laminar flame speed with time for ExF_1 flame and an equivalence ratio = 1, the hydrogen concentration of 20%, and 40%, the initial pressure of 1 atm and initial temperature of 298 K.

Fig. 11. The effect of the location of the ignition source on the equivalent laminar flame speed with time for 0 ms delay time and an equivalence ratio = 1, hydrogen concentration of 40%, the initial pressure of 1 atm and initial temperature of 298 K.

decreased. Fig. 9 illustrates the flame radius (z1) of the first external flame source (ExF_1) and the radius of the central flame radius on the ZZ axis (z) versus time for a wide range of equivalence ratio (0.8, 1, and 1.2) and the delay times (0, and 40 ms) to illustrate the flame–flame interaction as a matter of location and time.

Subsequently, the flame propagates with the fastest speed under stoichiometric conditions, the flames' interaction at the nearest location to the chamber's center and the minimum delay time. At zero delay time with an equivalence ratio of 1, and 1.2, the pressure wave slows and decelerates the flame speed, and the flame stabilizes at almost the same radius until the flames have interacted. As the delay time increases, the flame propagates appropriately, and the pressure wave advances beyond the flame front. However, when the equivalence ratio is 0.8, the influence is reversed; the deceleration and stabilization of the flame propagation occur at 40 ms. Otherwise, the flame propagates steadily across the delay time of 0 ms because of the low flame speed. Delay time significantly impacts the equivalent flame speed at stoichiometric conditions employing the first external flame source (ExF_1), as shown in Fig. 10. Since pressure waves influence flame propagation, it is seen that the equivalent flame speed decreases with increasing delay time. The equivalent flame speed propagates steadily initially, then drops significantly till the flames approach the interaction point. Increasing hydrogen blends increases the equivalent flame speed despite the delay time and increases the slope of decreasing flame speed.

Fig. 11 illustrates the equivalent flame speed versus time at stoichiometric conditions with a delay time of 0 ms at different external flames and a 40% hydrogen blend. It can be noticed that the equivalent flame speed decreases with time for both locations of ExF_1 and ExF_2 since the pressure wave traveled diagonally through the combustion chamber; also, the external flame was affected by the cold chamber wall. While the equivalent flame speed of the third external flame source (ExF_3) increases to a higher value than central because of the effect of the pressure wave in the same direction as the buoyancy effect.

Fig. 12 illustrates the influence of the equivalence ratio on the laminar burning velocity for different delay times and hydrogen blends using the first external flame (ExF_1). Additionally, applying three different mechanisms [38–40] to compare the laminar burning velocity with the centrally ignited flames for 20% and 40%. It can be observed that the maximum laminar burning velocity for a central flame and the corresponding flame from multi-ignition sources is found near stoichiometry and decreases on the lean and rich sides. Increasing the delay time at any stoichiometry and hydrogen blend prompts the combustion pressure and pressure wave to travel faster, reducing the
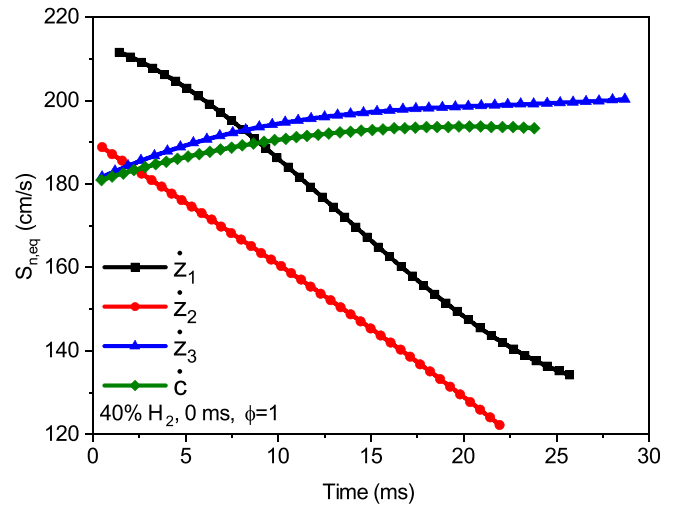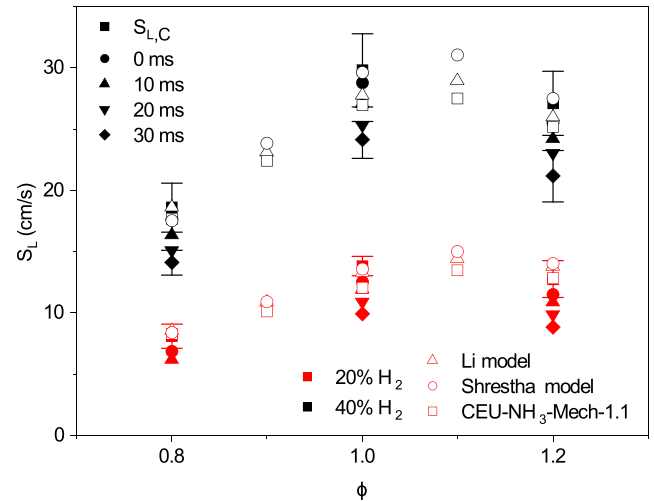

Fig. 12. Variation of the laminar burning velocity with equivalence ratio at different delay times for ExF_1 flame, and hydrogen concentration of, the initial pressure of 1 atm and initial temperature of 298 K.

time and location of the interaction; consequently, the flame speed and laminar burning velocity decrease.

Furthermore, it can be noticed that the effect of delay time on laminar burning velocity for the rich side is more evident with compare with the lean side. Besides, the effect of delay time on laminar burning velocity for the 40% hydrogen blend is more evident than for the 20% hydrogen blend.

Fig. 13 illustrates the laminar burning velocity versus delay time under stoichiometric conditions at different hydrogen blends and locations of external flames. It is noticeable that the laminar burning velocity for (ExF_1 and ExF_2) decreases with increasing delay time, but (ExF_3) increases with increasing delay time. Increasing the H_2 blend, the (ExF_1 and ExF_2) have positive L_b and would weaken in environments with significant stretch, but the (ExF_3) has a negative L_b and would accelerate. This thermo-diffusive flame reaction unavoidably impacts the performance of existing combustion systems.
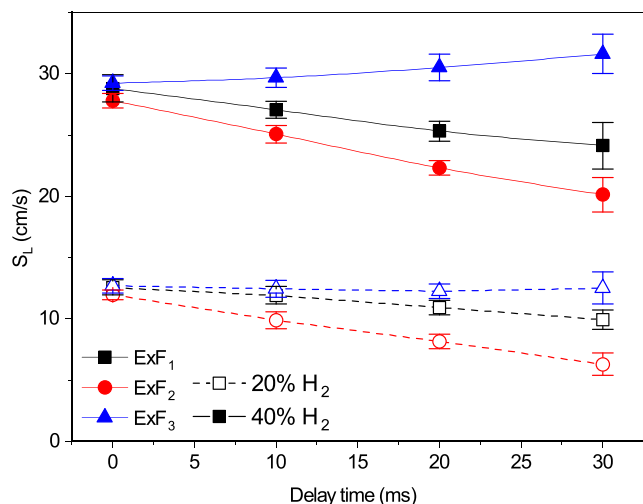
Fig. 13. The effect of the location of the ignition source on the laminar burning velocity with delay times at different hydrogen blending for an equivalence ratio = 1, the initial pressure of 1 atm and initial temperature of 298 K.

4. Conclusions

The characteristics of a premixed flame influence the flame propagation of energy convection devices or internal combustion engines. It is essential to understand how flame interaction affects ammonia–hydrogen premixed flames. To achieve this, the authors reviewed the investigations and application of hydrogen–ammonia fuels spherically expanding premixed flames. Experimentally, three locations on the right side of the combustion chamber have been chosen to study flame–flame interaction for spherically developing premixed flames. Besides, delay time and the equivalence ratio are investigated to find the effect on laminar flame morphology. The following conclusions are obtained;

1. A new method for extracting parameters related to the evolution of flame fronts and evaluating laminar flame propagation parameters in a constant volume chamber with multiple ignition sources has been proposed. The study involved comparing the flame morphology of a centrally-ignited hydrogen/ammonia/air flame under similar initial conditions. Prior to flame interaction, a pressure wave leads to deformation of the flame front, causing two opposing forces — drag force that slows down the flame and thrust force that accelerates its propagation. Additionally, the drag and lift forces caused by the pressure wave and buoyancy effect in the vertical direction also influence the shape of the expanding flame, resulting in a non-symmetric shape that changes from spherical to ellipsoidal and eventually to tri-axial quasi-ellipsoid flame (scalene).
2. By using the ignition source located on the lower right-hand side, the flame propagation on the upper and left sides increases. However, the flame propagation decreases in the right and downsides, as the flow is in the opposite direction of the propagation. Therefore, the equivalent flame speed reduces with time.
3. The flame speed is maximized at slightly rich conditions and decreases when it is either too lean or too rich. In the case of a rich condition, the external flame observed a cellular structure, while both flames in lean conditions showed cellularity and cracks due to the thinner flame thickness. Additionally, the speed of the single external flame at the third location (bottom direction) is higher compared to the centrally ignited flame because the pressure wave is in the same direction as the buoyancy.

4. Flame morphology may change due to several factors related to increasing the flame speed such as (hydrogen blend and equivalence ratio), or the delay time. For stoichiometric hydrogen–ammonia/air flames, as the delay time increases, the equivalent laminar flame speed decreases monotonously, as well as the time and location of interaction. For stoichiometric hydrogen–ammonia/air flames, the equivalent laminar flame speed is decreased with time for ignition sources 1 and 2. In contrast, the using of a third external flame source will increase the flame speed since the drag force is eliminated from the horizontal axis.
5. The laminar burning velocity is maximized near stoichiometry for all delay times and the location of the ignition source. Furthermore, for ignition sources 1 and 2, laminar burning velocity decreases with increasing delay time, and this becomes evident on the rich side. While employing a third ignition source, the laminar burning velocity increases with delay time. The hydrogen blending effect enhances and highlights this tendency.

5. Future outlook

Investigations using different fuel types (neat or blended) are commonly inadequate to gain insight into the complexity of combustion since changing different fuels requires selecting a matching delay time which depends on the size of the combustion chamber. Furthermore, studying how the delay time depends on the type of fuel being used is essential—investigations on the effect and quantifying flame morphology due to the buoyancy effect. Furthermore, studying the pressure history before and during flame interaction is interesting. Finally, cutting-edge image processing algorithms, such as deep learning algorithms, must be used further to investigate the flame volume calculations and their effect, examining the ultimate impact of local long and short flame cracks influenced by flame interaction.

CRediT authorship contribution statement

Ahmed Yasiry: Investigation, Conceptualization, Writing – original draft, Writing – review & edit. **Jinhua Wang:** Conceptualization, Funding acquisition, Methodology, Supervision, Writing – review & editing. **Hongchao Dai:** Validation, Visualization. **Xiao Cai:** Methodology, Writing – review & editing. **Ahmed A.A. Abdulraheem:** Visualization, Software. **Saba Y. Ahmed:** Investigation, Data Curation. **Haroun A.K. Shahad:** Methodology, Formal Analysis. **Zuohua Huang:** Funding acquisition, Supervision.

Declaration of competing interest

The authors declare that they have no known competing financial interests or personal relationships that could have appeared to influence the work reported in this paper.

Data availability

Data will be made available on request.

References

[1] Kobayashi Hideaki, Hayakawa Akihiro, Somarathne KD Kunkuma A, Okafor Ekenechukwu C. Science and technology of ammonia combustion. Proc Combust Inst 2019;37(1):109–33.

[2] Ritter James A, Ebner Armin D, Wang Jun, Zidan Ragaiy. Implementing a hydrogen economy. Mater Today 2003;6(9):18–23.

[3] Law Chung K. Combustion physics. Cambridge University Press; 2010.

[4] Elbaz Ayman M, Wang Shixing, Guiberti Thibault F, Roberts William L. Review on the recent advances on ammonia combustion from the fundamentals to the applications. Fuel Commun 2022:100053.

[5] Michalsky Ronald, Parman Bryon J, Amanor-Boadu Vincent, Pfromm Peter H. Solar thermochemical production of ammonia from water, air and sunlight: Thermodynamic and economic analyses. Energy 2012;42(1):251–60.

[6] Valera-Medina Agustin, Xiao Hua, Owen-Jones Martin, David William IF, Bowen PJ. Ammonia for power. Prog Energy Combust Sci 2018;69:63–102.

[7] Chai Wai Siong, Bao Yulei, Jin Pengfei, Tang Guang, Zhou Lei. A review on ammonia, ammonia-hydrogen and ammonia-methane fuels. Renew Sustain Energy Rev 2021;147:111254.

[8] Yapicioglu Arda, Dincer Ibrahim. A review on clean ammonia as a potential fuel for power generators. Renew Sustain Energy Rev 2019;103:96–108.

[9] Wang Zhi, Qi Yunliang, He Xin, Wang Jianxin, Shuai Shijing, Law Chung K. Analysis of pre-ignition to super-knock: Hotspot-induced deflagration to detonation. Fuel 2015;144:222–7.

[10] Ciniviz Murat, Köse Hüseyin. Hydrogen use in internal combustion engine: a review. Int J Automot Eng Technol 2012;1(1):1–15.

[11] Aleiferis Pavlos G, Rosati Martino F. Controlled autoignition of hydrogen in a direct-injection optical engine. Combust Flame 2012;159(7):2500–15.

[12] Wang Zhi, Liu Hui, Reitz Rolf D. Knocking combustion in spark-ignition engines. Prog Energy Combust Sci 2017;61:78–112.

[13] Zhen Xudong, Wang Yang, Xu Shuaiqing, Zhu Yongsheng, Tao Chengjun, Xu Tao, Song Mingzhi. The engine knock analysis–An overview. Appl Energy 2012;92:628–36.

[14] Pan Jiaying, Shu Gequn, Wei Haiqiao. Interaction of flame propagation and pressure waves during knocking combustion in spark-ignition engines. Combust Sci Technol 2014;186(2):192–209.

[15] Pan Jiaying, Shu Gequn, Zhao Peng, Wei Haiqiao, Chen Zheng. Interactions of flame propagation, auto-ignition and pressure wave during knocking combustion. Combust Flame 2016;164:319–28.

[16] Hariharan Ashwin, Wichman Indrek S. Structure and propagation of premixed flames in a closed combustion chamber with multiple ignition sources. Combust Sci Technol 2015;187(10):1562–83.

[17] Marchione Teresa, Ahmed Samer F, Mastorakos Epaminondas. Ignition of turbulent swirling n-heptane spray flames using single and multiple sparks. Combust Flame 2009;156(1):166–80.

[18] Zheng Kai, Song Chen, Yang Xufeng, Wu Jie, Jiang Juncheng, Xing Zhixiang. Effect of obstacle location on explosion dynamics of premixed H2/CO/air mixtures in a closed duct. Fuel 2022;324:124703.

[19] Xiao Huahua, Duan Qiangling, Jiang Lin, Sun Jinhua. Effects of ignition location on premixed hydrogen/air flame propagation in a closed combustion tube. Int J Hydrogen Energy 2014;39(16):8557–63.

[20] Tyagi Ankit, Boxx Isaac G, Peluso Stephen J, Shupp Ryan, O'Connor Jacqueline. Structure of flames in flame interaction zones. In: 2018 AIAA aerospace sciences meeting. 2018, p. 0161.

[21] Dunstan TD, Swaminathan N, Bray KNC, Kingsbury NG. Flame interactions in turbulent premixed twin V-flames. Combust Sci Technol 2013;185(1):134–59.

[22] Dunstan TD, Swaminathan N, Bray KNC, Kingsbury NG. The effects of non-unity lewis numbers on turbulent premixed flame interactions in a twin V-flame configuration. Combust Sci Technol 2013;185(6):874–97.

[23] Xu Leilei, Fan Qingshuang, Liu Xin, Cai Xiao, Subash Arman Ahamed, Brackmann Christian, Li Zhongshan, Aldén Marcus, Bai Xue-Song. Flame/turbulence interaction in ammonia/air premixed flames at high karlovitz numbers. Proc Combust Inst 2022.

[24] Wijeyakulasuriya Sameera D, Rajagopal Manikanda, Nalim Razi. Shock-flame interaction modeling in a constant-volume combustion channel using detailed chemical kinetics and automatic mesh refinement. In: Turbo expo: power for land, sea, and air. Vol. 55102, American Society of Mechanical Engineers; 2013, V01AT04A042.

[25] Wijeyakulasuriya Sameera D, Mitra Saurav. Analyzing three-dimensional multiple shock-flame interactions in a constant-volume combustion channel. Combust Sci Technol 2014;186(12):1907–27.

[26] Arcoumanis C, Bae C-S. Visualization of flow/flame interaction in a constant-volume combustion chamber. SAE Trans 1993;102:1227–40.

[27] Bradley D, Kalghatgi GT, Golombok M, Yeo Jinku. Heat release rates due to autoignition, and their relationship to knock intensity in spark ignition engines. In: Symposium (international) on combustion. Vol. 26, Elsevier; 1996, p. 2653–60.

[28] Oppong Francis, Luo Zhongyang, Li Xiaolu, Song Yang, Xu Cangsu. Intrinsic instability of different fuels spherically expanding flames: A review. Fuel Process Technol 2022;234:107325.

[29] Abdulraheem Ahmed AA, Saleh Adel M, Shahad Haroun AK. Experimental study on the unstretched laminar flame speed and markstein length of premixed methanol/air flames at different initial temperatures and pressures. Des Eng 2021;13357–73.

[30] Chen Zheng. On the accuracy of laminar flame speeds measured from outwardly propagating spherical flames: Methane/air at normal temperature and pressure. Combust Flame 2015;162(6):2442–53.

[31] Moffat Robert J. Describing the uncertainties in experimental results. Exp Therm Fluid Sci 1988;1(1):3–17.

[32] Lhuillier Charles, Brequigny Pierre, Lamoureux Nathalie, Contino Francesco, Mounaïm-Rousselle Christine. Experimental investigation on laminar burning velocities of ammonia/hydrogen/air mixtures at elevated temperatures. Fuel 2020;263:116653.

[33] Bradley Derek, Gaskell Philip H, Gu Xiao-Jun. Burning velocities, markstein lengths, and flame quenching for spherical methane-air flames: a computational study. Combust Flame 1996;104(1–2):176–98.

[34] Burke Michael P, Chen Zheng, Ju Yiguang, Dryer Frederick L. Effect of cylindrical confinement on the determination of laminar flame speeds using outwardly propagating flames. Combust Flame 2009;156(4):771–9.

[35] Kreyszig Erwin. Advanced mathematics for engineering and science. 2006.

[36] Jomaas Grunde, Law Chung King, Bechtold JK. On transition to cellularity in expanding spherical flames. J Fluid Mech 2007;583:1–26.

[37] Chen Xu, Liu Qingming, Jing Qi, Mou Zonglei, Shen Yang, Huang Jinxiang, Ma Hongrong. Flame front evolution and laminar flame parameter evaluation of buoyancy-affected ammonia/air flames. Int J Hydrogen Energy 2021;46(77):38504–18.

[38] Wang Shixing, Wang Zhihua, Chen Chenlin, Elbaz Ayman M, Sun Zhiwei, Roberts William L. Applying heat flux method to laminar burning velocity measurements of NH3/CH4/air at elevated pressures and kinetic modeling study. Combust Flame 2022;236:111788.

[39] Li Rui, Konnov Alexander A, He Guoqiang, Qin Fei, Zhang Duo. Chemical mechanism development and reduction for combustion of NH3/H2/CH4 mixtures. Fuel 2019;257:116059.

[40] Shrestha Krishna P, Seidel Lars, Zeuch Thomas, Mauss Fabian. Detailed kinetic mechanism for the oxidation of ammonia including the formation and reduction of nitrogen oxides. Energy Fuels 2018;32(10):10202–17.